Monte Carlo simulations of water pollutant adsorption at parts-per-billion concentration: A study on 1,4-dioxane

Samiha Sharlin,[*,†] Rodrigo Lozano,[‡] and Tyler R. Josephson[*,†,¶]

†*Department of Chemical, Biochemical, and Environmental Engineering, University of Maryland Baltimore County*

‡*Department of Chemistry, University of California Irvine*

¶*Department of Computer Science and Electrical Engineering, University of Maryland Baltimore County*

E-mail: s126@umbc.edu; tjo@umbc.edu

Abstract

1,4-dioxane is an emerging water pollutant with high production volumes and a probable human carcinogen. The incompetence of conventional treatment processes demonstrates a need for an effective remediation strategy. Crystalline nanoporous materials are cost-effective adsorbents due to their high capacity and selective separation in mixtures. This study explores the potency of *all-silica* zeolites. These zeolites are highly hydrophobic and can preferentially adsorb nonpolar molecules from mixtures. We investigated six zeolite frameworks (BEA, EUO, FER, IFR, MFI, MOR) using Monte Carlo simulations in the Gibbs ensemble. The simulations indicate high selectivity by FER and EUO, especially at low pressures, which we attribute to pore sizes and shapes with more affinity to 1,4-dioxane. We also demonstrate a Monte Carlo simulation

workflow using gauge cells to model the adsorption of an aqueous solution of 1,4-dioxane at 0.35 ppb concentration. We quantify 1,4-dioxane and water coadsorption, and observe selectivities ranging from 1.1 x 10^5 in MOR to 8.7 x 10^6 in FER. We also demonstrate that 1,4-dioxane is in the infinite dilution regime in both the aqueous and adsorbed phases at this concentration. This simulation technique can be extended to model other emerging water contaminants such as per- and polyfluoroalkyl substances (PFAS), chlorates, and others, which are also found in extremely low concentrations.

1 Introduction

Crystalline porous materials like metal-organic frameworks (MOFs), covalent organic frameworks (COFs), carbon nanotubes, polyoxometalates, and zeolites, have revolutionized mixture adsorption separations through control of pore size[1], entropy[2], and binding strength[3]. Additionally, their stability, tunability, and low cost make them versatile[4] - for example, zeolites are used as catalysts[5], adsorbents[6], and ion exchangers[7] in many chemical processes and have an increasingly rising global market of multi-billion US dollars[8]. Water and wastewater remediation methods also extensively use zeolites for purification from ammonia[9], heavy metals[10], radioactive[11], toxic[12], and organic substances[13], for water softening[14] and seawater desalination[15].

The basic building block of zeolites is a TO_4 tetrahedron where the T-atom is usually silicon (Si) or aluminum (Al), forming an open crystal structure with small pore size and distribution. The tetrahedrons can form different (6-, 8- or 12 rings) units that give different topologies with the same chemical composition[16]. Over 40 naturally occurring zeolite frameworks and over 253 synthetic ones are recognized by the International Zeolite Association (IZA) Structure Commission as of December 2018[17]. Zeolites with a high silicon content (approaching an infinite Si/Al ratio) can be synthesized;[18,19] because this class of zeolites doesn't have acid sites or polar cations, they can be highly hydrophobic and are exceptionally efficient as adsorbents in aqueous separations[13,20].

This study investigates the adsorption of 1,4-dioxane from water using all-silica zeolites at environmental concentrations using molecular simulations. 1,4-dioxane is an emerging contaminant and a probable human carcinogen[21] that has received less regulatory attention than other pollutants despite being frequently detected in high exceedance rates according to the third unregulated contaminant monitoring rule (UCMR)[22]. It is a stable cyclic diether with symmetrical ether connections. A negative octanol-water partitioning coefficient and low carbon partitioning coefficient make leaching into the water from soil natural[23]. Recent studies show that over 30 million Americans consume water exceeding the health-based recommended threshold of 0.35 ppb[24]. To comply with the standards, several remediation strategies, including chemical, physical, and biological processes, are being evaluated; however, a practical solution for large-scale treatment is still in the works[23]. While enhanced oxidation and bio-remediation techniques have potential, they are costly and complicated to execute in practical settings[25]. As degradation technologies are still developing, considerable mitigation efforts may well focus on treating surface and groundwater bodies to comply with the increasingly stringent limits to drinking water supplies. While these methods might fail to degrade water pollutants entirely, they can act as an interim that can potentially concentrate contaminants for subsequent remedial actions needed.

Common adsorbents like synthetic resins[26] and activated carbon[27] have not been cost-effective solutions for large-scale treatment of 1,4-dioxane due to their limited adsorptive capacity. Meanwhile, in one study, titanium silicalite-1, a zeolite, has shown higher capacity and faster adsorption kinetics due to its hydrophobicity[28]. Hydrophobic all-silica zeolites with comparable pore sizes may help address this challenge, but more insight is needed to determine its efficacy. For our investigation, we selected six frameworks (BEA, EUO, FER, IFR, MFI, and MOR) from the International Zeolite Association database[17] based on their commercial availability[29], crystallographic R-factor in high silica form[30], and pore sizes comparable to 1,4-dioxane[28]. The pore landscapes of the zeolites are shown in Figure 10, and Table 4 summarizes their unit cell parameters.

The optimal design of an adsorbent is a challenging task and requires a broad understanding of the sorption process at the microscopic level. Molecular simulations complement and provide invaluable access to thermodynamic phenomena occurring at the pore sites and thus have significantly contributed to the synthesis and applications of zeolite[16,31,32]. Additionally, adsorption systems with competition between complex adsorbates onto complex adsorbents can be better understood and more clearly evaluated through computer simulations[33,34]. For example, molecular dynamics has been used to study 1,4-dioxane transport and adsorption into Ti-silicalite in the presence of organic contaminants[28].

However, the traditional simulation approach for sampling such a system is not only impractical but impossible since the concentrations of 1,4-dioxane in the environment are typically in parts per billion ranges[24]. For instance, we would need a liquid simulation box of 200 million $Å^3$ to accommodate this low concentration. This work introduces a simulation workflow using the gauge cell Monte Carlo (gcMC) technique to efficiently model the liquid phase adsorption of extremely low-concentration species from mixtures. The gcMC method enables control of density for each system component individually and has successfully modeled the thermodynamically metastable and unstable systems that are typically inaccessible[35–38]. The method has been successfully implemented to investigate the phase behavior of fluids in confined spaces, including capillary condensation[39], droplet formation[37,40], and surfactant separation[41].

In a study by Luo and Farrel[42], the adsorption of trichloroethylene (TCE) from water was examined using Grand Canonical Monte Carlo (GCMC) simulations. They sampled TCE in aqueous solution at concentrations equivalent to 1% of its saturation concentration. This study extends to sampling water contaminants at parts-per-billion levels, which is typical of environmental conditions. While we apply this approach using Gibbs ensemble simulations, we note that it should also be compatible with simulations in the grand canonical ensemble, with a few modifications. The thermodynamic reservoir fixing the chemical potential will replace the gauge cells, and extrapolation will be performed by adjusting the

chemical potential of the solute accordingly after establishing the relationship between μ and concentration in infinite dilution conditions. Performing GCMC simulations at the pressure of interest for the liquid mixtures will require iteratively adjusting simulation settings until the target pressure is reached, as GCMC fixes μVT and measures p, unlike our approach, which fixes NpT and measures μ.

We performed Monte Carlo simulations in the Monte Carlo for Complex Chemical Systems - Minnesota (MCCCS-MN) software[43] using classical force fields. First, we reproduced the vapor-liquid equilibrium properties of 1,4-dioxane for validation and then simulated the vapor and liquid phase adsorptions of 1,4-dioxane into the selected zeolite frameworks. The pure adsorption isotherms provided insight into the effects of pore size and shape on loading capacities. Finally, we investigated the selectivity of 1,4-dioxane for mixture adsorptions in water at the health-based reference concentration (0.35 ppb), exploiting the gauge cell method and constructing supercell unit volumes for the zeolite frameworks.

2 Methods

2.1 Thermodynamic extrapolation approach

The gcMC method employs multiple simulation boxes, with one primary cell for the system of interest in chemical equilibrium with gauge cells for each component. The primary cell is flexible and modeled as a real system with intermolecular interactions, while the gauge cells are rigid and treated as ideal gas boxes. The addition or removal of particles from the gauge cell instantly changes its chemical potential, and it is this variation that enables us to measure the chemical potential of the species in the main cell under conditions of interest.

The simulations were set up isobaric–isothermal Gibbs ensemble (NpT-Gibbs)[44–46] where inter-box swaps were performed for the particles between the main cell and gauge cell of each respective component. Volume moves were only performed on the main cell representing the mixture solution. The Gibbs free energy of transfer, ΔG^{*0}_{14DX},[47,48] for 1,4-dioxane can be

computed from the ratio of densities in the simulation boxes:

$$\Delta G^{*0}_{14DX} = kT\Big[\ln\Big(\frac{\rho^{GC}_{14DX}}{\rho^{mix}_{14DX}}\Big)_{eq}\Big] \tag{1}$$

where k, T, ρ^{GC}_{14DX}, ρ^{mix}_{14DX} are Boltzmann constant, temperature, and number density of 1,4-dioxane in gauge cell and mixture cell respectively. A detailed derivation of Eq. 1 can be found in SI section 5.3. We used Eq. 1 to determine the free energy of transfer for the dilute system of 1,4-dioxane. For extrapolation, we took the average ΔG^{*0}_{14DX} of low-concentration state points and computed the 1,4-dioxane concentration in gauge cell that would correspond to 0.35 ppb[24] in the environment. Since the concentration range is exceptionally low, we used Henry's Law to compute the corresponding pressure. Then, we set up NpT-Gibbs ensemble simulations with zeolite frameworks to model adsorption from low-concentrated liquid mixtures.

2.2 Model and algorithmic details

Transferable potentials for phase equilibria (TraPPE)[49] force fields were used to model 1,4-dioxane with TraPPE-UA[50], and the zeolites were modeled using TraPPE-zeo[51]. Lennard-Jones (LJ) potentials were used for short-range van der Waals interactions, and Coulomb potentials were used for long-range electrostatic interactions with a spherical cutoff of 14 Å. Beyond this cutoff, analytical tail corrections were applied for LJ and Ewald summation for Coulomb interactions. However, the vapor box was less dense for lower temperature state points, and thus, a larger cutoff (approximately 30% of box length) was used.

As with the standard TraPPE force fields, here the bond lengths were treated as fixed, bend angles were modeled with the simple harmonic oscillator, and the dihedrals with a cosine series (Eq. 2) of the form

$$u_{\text{torsion}}(\phi) = c_0 + c_1\left[1 + \cos(\phi)\right] + c_2\left[1 - \cos(2\phi)\right] + c_3\left[1 + \cos(3\phi)\right] \tag{2}$$

where ϕ is the dihedral angle and c is constant.

The TraPPE-zeo model considers zeolites as a rigid framework with silicon and oxygen atoms fixed on the original crystallographic positions. Their interaction potentials are tabulated as grid points, which can be interpolated to give energy depending on the location of adsorbent species in the simulation boxes. Additionally, TIP4P model was used for water[52] in the mixture adsorption systems as it has been shown to work well with the TraPPE force field for organic molecules[51,53–57]. All the model parameters used for this study are summarized in Table 5 of Supplementary section 5.2. The adsorption simulations were initialized with an empty zeolite box to prevent overlap issues for both unary and mixture systems.

Simulations were performed in NVT-Gibbs ensemble for modeling the vapor-liquid equilibrium properties, and NpT-Gibbs was used for both adsorption and gauge cell systems[44–46]. Monte Carlo simulations generate a sequence of states as a Markov chain with sampling probabilities corresponding to the ensemble's configurational integral[58,59]. Intramolecular and intermolecular energies are sampled efficiently using strategic Monte Carlo moves, which are constrained by their alignment with the chosen ensemble and their adherence to the detailed balance defined by the Metropolis acceptance criteria[60].

Gibbs ensemble consists of two (or more) simulation boxes with a constant total number of molecules without explicit interfaces. In such a system, the inter-box swap move is integral to balance the chemical potentials in addition to the regular translation, rotation, and volume moves. Configurational-bias Monte Carlo (CBMC)[61–63] moves were also employed to sample configurations within each simulation box, as well as inter-box swap moves. In regular CBMC, a molecule is grown bead by bead, with `k` trial positions generated based on the internal energy for each bead, and the external energy is computed for each trial position `j` of each bead `i`. One of these trial positions is selected and added to the existing chain with a probability of:

$$P_i(j) = \frac{e^{-\beta U_i^{ext}(i)}}{\sum_{l=1}^{k} e^{-\beta U_i^{ext}(i)}} \tag{3}$$

and $\beta = 1/k_B T$ where k_B is the Boltzmann constant and T is the temperature[64].

The process repeats until the entire molecule is grown. Various approaches to CBMC exist in the literature[62,63,65–68], each with a different method of bead growth tailored to specific conformations of molecules. 1,4-dioxane, for instance, is challenging to grow with regular CBMC because the ring structure constrains its conformational space. The growth of such cyclic molecules requires an additional bias to nudge the growth toward positions that will result in ring closures; here, we use the self-adapting fixed-endpoint (SAFE) CBMC developed by Wick and Siepmann[69]. The bias was introduced through guiding probabilities obtained from a short presimulation with only the translational and rotational degrees of freedom. The probabilities are normalized ensemble averaged bead-bead distance distributions that adapt during the simulation of the system of interest. Thus, the swap moves for 1,4-dioxane were performed holding the ring conformation rigid while allowing multiple trial orientations to be explored.

2.3 Super cell construction

Each zeolite framework has a building unit that repeats to form a three-dimensional lattice structure. For instance, the FER (type 2) framework has two repeating units in the x-direction, four in the y-direction, and two in the z-direction, making up a minimal simulation cell. This ensures the simulation box side lengths are at least twice the cutoff radius (28 Å) and allows the implementation of periodic boundary conditions with the minimum image convention. Apart from the minimal simulation cell frameworks, we constructed supercells by multiplying a factor of 2, 4, and 8 in all three dimensions and analyzed selectivity across cell volumes. Figure 1 shows the scheme of supercell construction for the FER framework. For simplicity, we only show a single unit cell of FER, its minimal simulation cell, and the

largest supercell (minimal simulation cell × 512) used as the zeolite simulation box in mixture adsorption systems. As the interactions within the zeolite frameworks are pretabulated, we can easily increase the zeolite simulation box size to model the supercells without incurring additional computational costs.

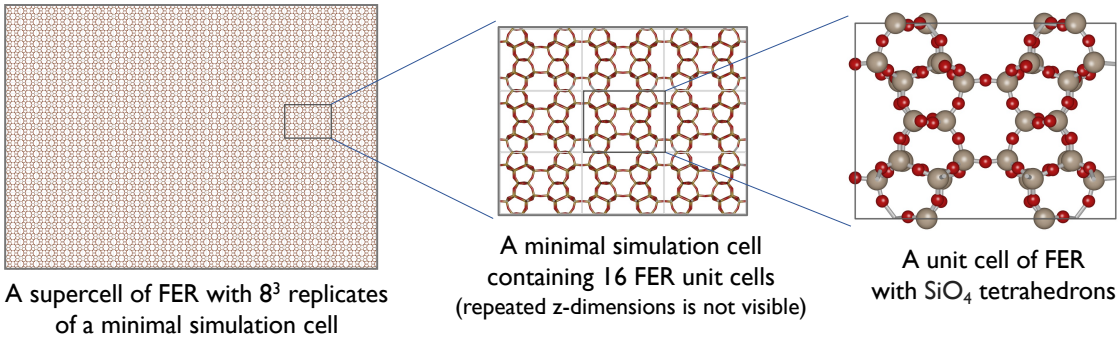

Figure 1: Scheme of supercell construction

3 Results and Discussion

3.1 Force field validation for 1,4-dioxane

Before running adsorption simulations with 1,4-dioxane, we validated the force fields against simulation[50] and experimental data[70] from literature (Figures 2a and 2b). To estimate the statistical uncertainties in the coexistence properties, 16 independent simulations were performed for temperatures ranging from 310 K to 565 K with 80k MC cycles for equilibration and 100k MC cycles for production. The total volume of the two simulation boxes was adjusted so that the vapor phase contained roughly 50 molecules, which accounts for about 10% of the total system size of 500 molecules. Our findings closely resemble simulated data in the literature and reasonably agree with experimental data. The critical temperature is overestimated by approximately 0.7%, and the normal boiling temperature is underestimated by 3.5%. The underestimation of normal boiling temperature is systematic in TraPPE-UA models[71] as they also tend to predict higher saturated vapor densities and pressures.

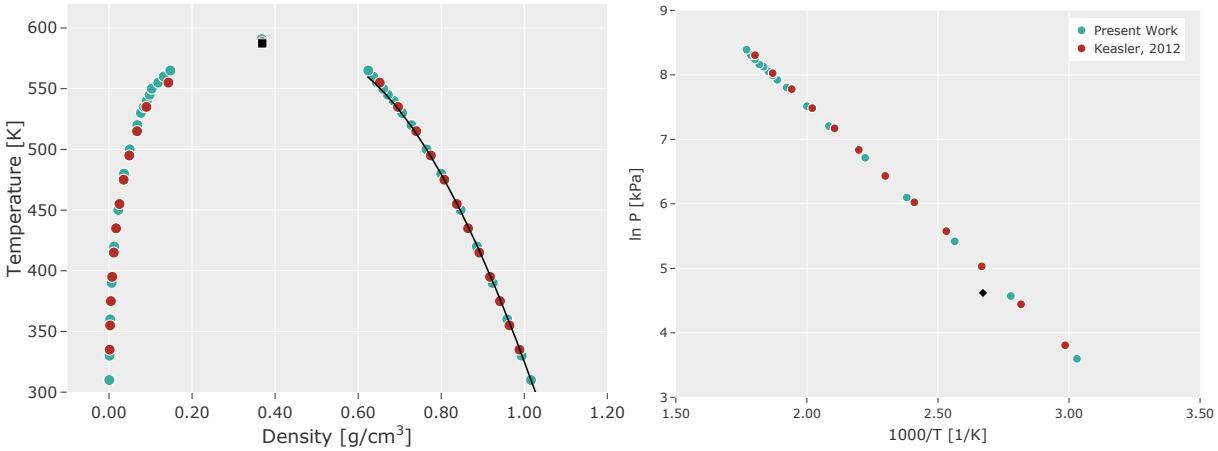

(a) Vapor-liquid coexistence curve

(b) Clausius Clapeyron plot

Figure 2: Vapor-liquid coexistence curves and Clausius Clapeyron plot for 1,4-dioxane. Experimental critical temperature (■T_c) and data, including normal boiling temperature (◆T_b), are shown in black symbols and solid lines. Simulation uncertainties are smaller than symbol size.

3.2 Unary adsorption loadings for 1,4-dioxane

Single-component adsorption was studied at 300 K for 1,4-dioxane for a range of pressures, with the upper limit for vapor phase adsorption set to 0.05 bar so as not to exceed the saturation pressure (p_{vap}) of 1,4-dioxane at 300 K, which is approximated from simulations to be 0.105_3 bar. Two state points beyond p_{vap} were used to model adsorption from a liquid phase. The fluid box was initialized as a low-density gas at low pressures ($p < p_{\text{vap}}$), or as a high-density liquid at higher pressures ($p > p_{\text{vap}}$) to prevent nucleation issues. Eight independent simulations were performed for each framework with at least 80k equilibration and 100k production cycles. Some of the frameworks required more time to reach equilibration, especially for higher pressure state points, but no simulations exceeded 500k MC cycles. We used an automated equilibrium detection technique to determine which portion of the simulation runs from production cycles to use for reporting results described by Chodera[72]. The technique determines the optimal amount of initial data that needs to be discarded to equilibration for molecular simulations while minimizing initial bias and variance. The pure 1,4-dioxane adsorption isotherms for the six zeolite frameworks are

plotted in Figure 3.

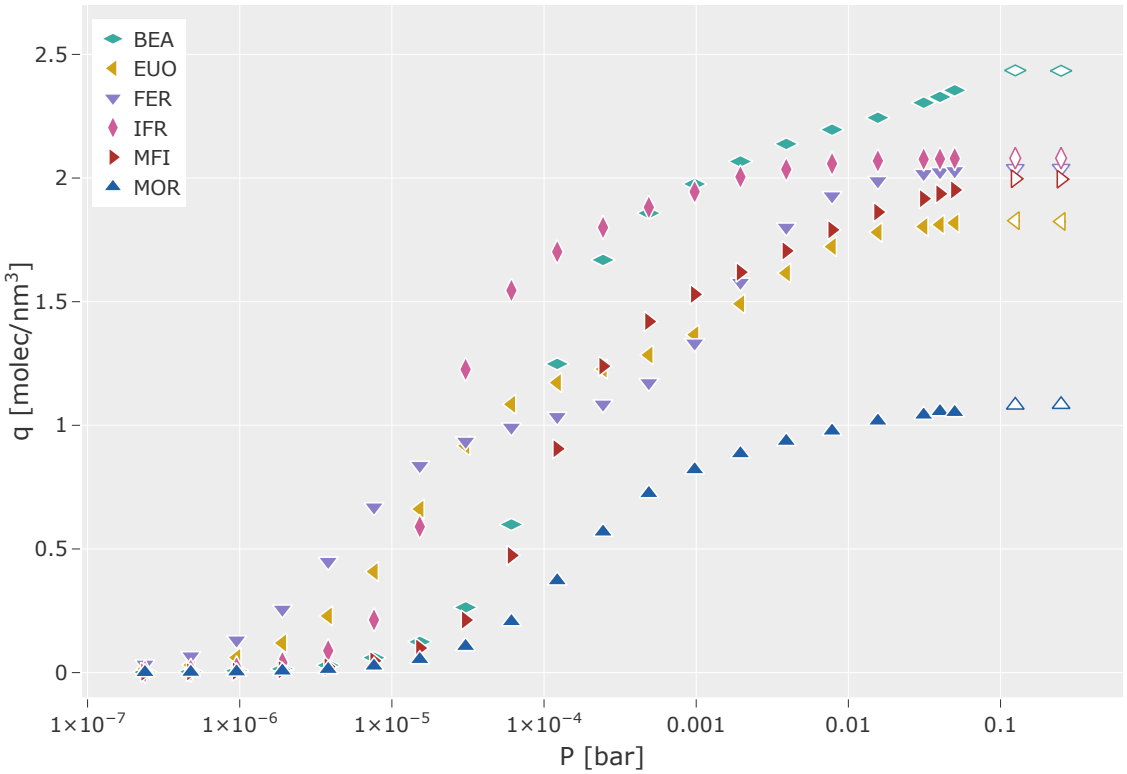

Figure 3: Predicted unary adsorption isotherms. The y-axis represents loadings (q) for six zeolite frameworks with pressure in the x-axis (logarithmic scale). Open symbols indicate adsorption from a liquid phase. Simulation uncertainties are smaller than symbol size.

The loading capacities for 1,4-dioxane at higher pressure are in the following order: BEA > IFR > FER > MFI > EUO > MOR. Frameworks with high-loading capacities like BEA or IFR may seem to be an optimal choice for an adsorbent as literature studies with other adsorbent materials have reported that capacity is a limiting factor[26–28].

However, our focus here is on modeling the adsorption behavior in environmental

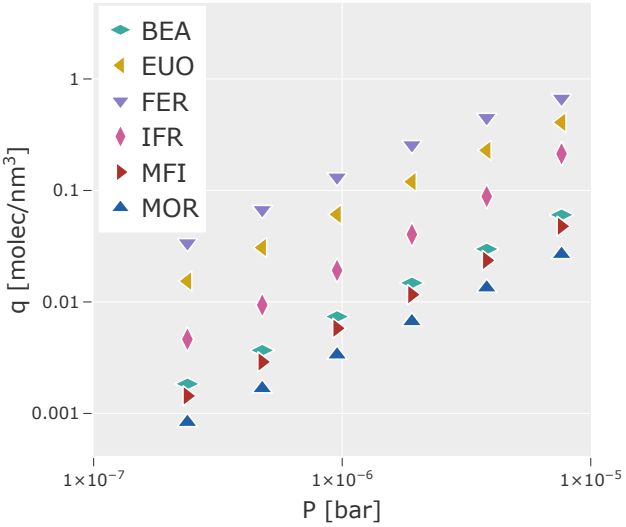

Figure 4: Inset view of Figure 3. Here both loading and pressure are plotted on a logarithmic scale to visualize the data points clearly.

conditions where 1,4-dioxane is found in
low concentrations. Lower pressures correspond to low chemical potentials and low concentrations, and we observe upon closer inspection (Figure 4) that FER performs significantly better than the others in these low-pressure regions.

At lower pressures, the adsorption process is mainly driven by affinity, which is driven by interactions with the pores, due to pore size and shape. Simulation snapshots show that 1,4-dioxane preferentially adsorbing into the smaller 8-membered ring of the FER framework at low pressures, as shown in Figure 5. The 8-ring pore of FER and 1,4-dioxane form a snug fit, which is a crucial factor for selectivity in adsorption of mixtures. An investigation on the adsorption of 1-butanol and water across distinct pore channels demonstrated how water coadsorption is specifically related to pore size[73]. Various other adsorption separation systems, including xylene isomers in MFI[74] and ethane/ethylene separations[75], also show when pore size and adsorbate molecules exhibit close conformity, the scope for coadsorption is considerably restricted. However, as the Monte Carlo simulation trajectories are generated stochastically and include swap moves that directly insert molecules into the pores, these simulations cannot verify whether 1,4-dioxane molecules can diffuse through the surface to reach the smaller 8-ring pores of FER.

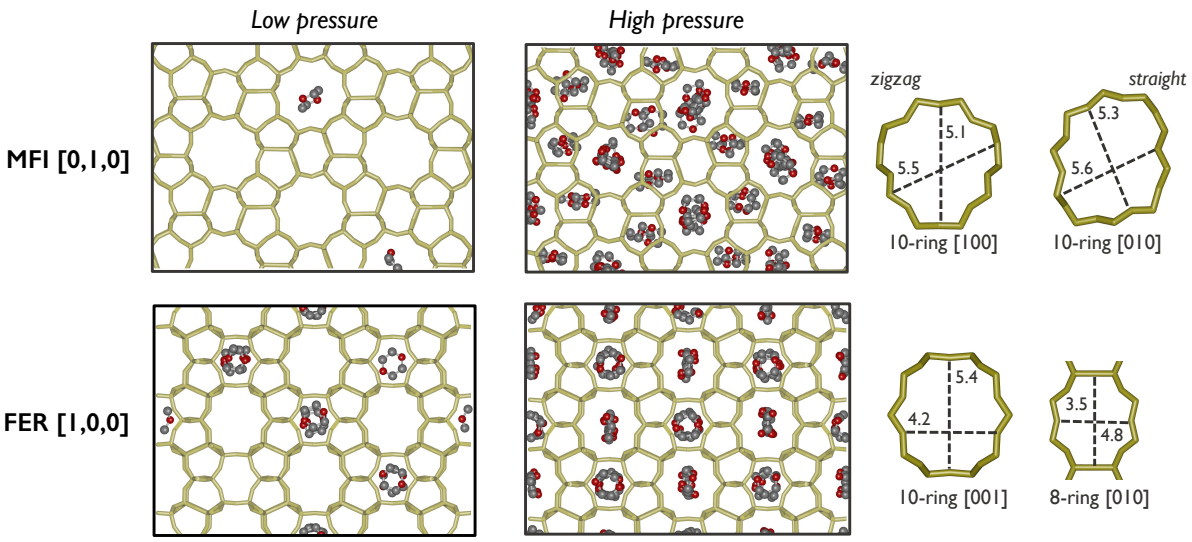

Figure 5: Loading of 1,4-dioxane at pore sites. Snapshots illustrating the loading of 1,4-dioxane in MFI (top row) and FER (bottom row) frameworks at low and high pressures.

3.3 Mixture adsorption at environmental concentrations

We conducted a small test (NpT-Gibbs simulation with 120 1,4-dioxane and 600 water molecules at 1 atm and 300 K) to determine if all-silica zeolites efficiently separate 1,4-dioxane from water under environmentally relevant conditions. While the test results were promising (we observed selective adsorption of 1,4-dioxane, with just about 14 molecules remaining in the liquid phase), we quickly realized that our simulation conditions were far from the parts per billion concentrations needed to model environmental conditions. Replicating the concentration of 1,4-dioxane that is considered safe for human health, i.e., 0.35 ppb (micrograms per liter of water), we would require approximately 100 million water molecules for every molecule of 1,4-dioxane. Sampling with a regular NpT-Gibbs ensemble for such a system is not only impractical but also computationally inefficient, so we developed an approach using gauge cells and extrapolation as shown in Figure 6.

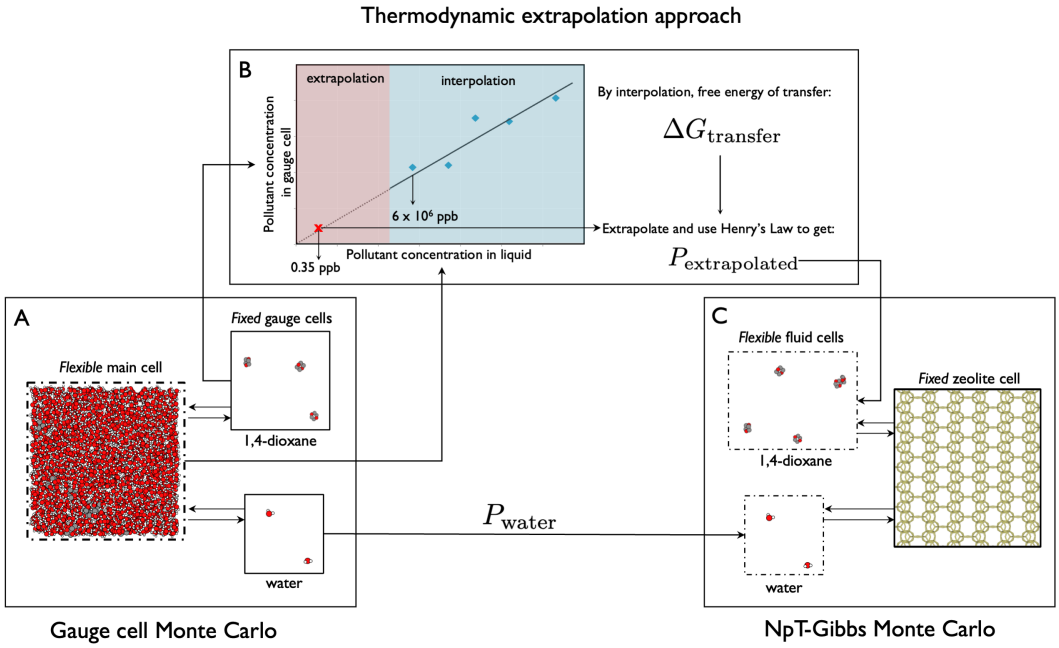

Figure 6: Thermodynamic extrapolation approach for dilute simulations. The first step (A) involves gauge cell Monte Carlo simulations with a dilute solution of 1,4-dioxane and water in the main cell, in chemical equilibrium, with two fixed ideal gas gauge cells that measure the partial pressures of 1,4-dioxane and water. We adjust the size of the 1,4-dioxane gauge cell to sample low concentrations in the main cell. The second step (B) involves obtaining the free energy of transfer from low-concentration state points, demonstrating the solute is in the Henry's law regime, then assuming that $\Delta G_{\text{transfer}}$ extrapolates to 0.35 ppb concentration. The 1,4-dioxane concentration in the gauge cell is calculated from Equation 1, and the ideal gas law provides the extrapolated partial pressure. In the final step (C), NpT-Gibbs simulations use the extrapolated pressure for 1,4-dioxane while keeping the water pressure constant, thus imposing the equivalent chemical potentials of the dilute mixture onto a zeolite box.

3.3.1 Gauge cells and thermodynamic extrapolation

We performed simulations with 30 1,4-dioxane and 1800 water molecules, and we obtained different fluid concentrations by setting the 1,4-dioxane gauge cell size to varying volumes, from 100^3 Å^3 to 310^3 Å^3. However, when we increased the simulation box side length beyond 310 Å, all of the 1,4-dioxane left the gauge cell simulation box, so no statistically meaningful concentration remained. We adjusted the water gauge cell size to enable swaps of approximately 4 water molecules between the main cell. We then fixed the water gauge cell size for all the state points analyzed by increasing the 1,4-dioxane gauge cell size.

Since the system under investigation is at a low temperature (300 K), we faced sampling challenges in particle insertions. We had swap acceptance rates of about 0.001, even while considering 32 trials for insertion and 16 orientational trial positions. A drawback of using this gauge cell approach over traditional NpT-Gibbs is we also can not implement identity switch moves to boost sampling efficiency.

For each state point, eight independent simulations were conducted with a minimum of 400k MC cycles; and some state points required up to 500k cycles to equilibrate. While separate production runs were not performed for this setup, we used Chodera's equilibration detection method[72] to determine the regime of the data deemed to represent equilibrium. We determined the mean free energy of transfer for 1,4-dioxane at the six lowest concentrations in the main cell, as shown by the data points to the left of the black dashed line in Figure 7 and Table 1. Using that free energy and health-based reference concentration in Equation 5.3, we compute the 1,4-dioxane concentration in the gauge cell. Applying Henry's law for this concentration, we obtained a corresponding pressure of 5.8×10^{-11} bar for 1,4-dioxane. The Supplementary section 5.4 includes the plot of pressure versus concentration, along with step-wise calculations for extrapolation. The pressure in the gauge cell of water is the average across the state points and is 4.5×10^{-2} bar. We finally use these pressures for 1,4-dioxane and water to set up NpT-Gibbs simulations at 300 K and model adsorption with 50 1,4-dioxane molecules and up to 1600 water molecules.

N_{14DX}^{mix}	ρ_{14DX}^{mix} [molec/nm^3]	ΔG_{14DX}^{*0} [kJ/mol]
2.3_3	0.035_5	-8.8_5
2.7_3	0.042_5	-9.3_3
3.8_4	0.060_7	-9.8_4
4.3_5	0.067_7	-9.2_3
5.6_2	0.087_4	-9.0_6
6.8_3	0.106_4	-8.8_5

Table 1: Free energy of transfer for the lowest six state points. The average free energy is $\overline{\Delta G_{14DX}^{*0}} = -9.2$ kJ/mol. The subscripts report uncertainty to the last significant figures of the mean values.

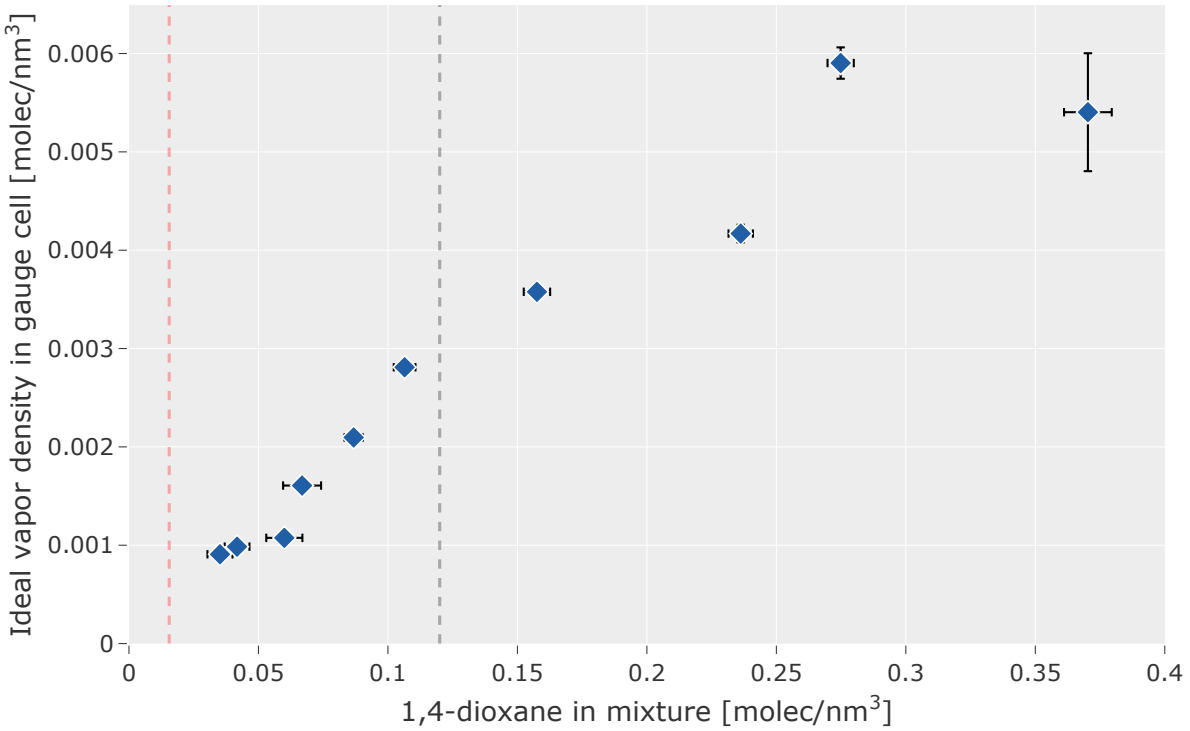

Figure 7: 1,4 dioxane concentration in gauge cell versus in the main cell. The six lowest data points, to the left of the black dashed line, were used to calculate the change in Gibbs free energy (ΔG). The red dashed line represents the point where the main cell contains only one 1,4-dioxane molecule.

We used a series of gauge cell simulations in order to validate that we are in the infinite dilution regime. A more efficient approach would be to perform gauge cell simulations at just one concentration (as low as possible) and obtain free energy of transfer (ΔG) from this. By using a series of simulations, however, we established that this system is in the Henry's law (infinite dilution) regime. While we are not <1 molecule / simulation box, the trend of the state points suggests we are not seeing significant 1,4-dioxane — 1,4-dioxane interactions.

When we impose the extrapolated 1,4-dioxane partial pressure and the water partial pressure on the zeolite box, our state point will be at a slightly lower total pressure than the 1 atm that was fixed thermodynamically in the gauge cell simulations due to the loss of some 1,4-dioxane. We anticipate this will be a minor effect, given the low concentrations.

An alternative method for obtaining a water partial pressure for the extrapolated system is to measure this in a system of pure water instead of obtaining it from systems with small amounts of solute.

3.3.2 Selectivity in Mixture Adsorptions

Mixture adsorption experiments were conducted across all zeolite frameworks using four different setups. Each setup had increasing minimal simulation cell volumes that were scaled by a factor of 8 to create supercells, as shown in Figure. 1. This approach enabled us to effectively sample 1,4-dioxane at extremely low loadings of parts per billion concentrations in water.

Eight independent simulations were conducted for each zeolite framework setup, with 180k equilibration and 120k production cycles. Figure 8 illustrates the loading per unit volume of zeolites across different unit cell sizes. FER exhibits the best performance among all the zeolites, followed by EUO, IFR, BEA, MFI, and MOR. A notable increase in loading is observed when the unit cell is scaled up by a factor of 2^3 times the unit cell volume, with FER demonstrating the most significant improvement. Scaling the unit cell beyond this point does not result in much performance gain.

The mixture adsorption loadings follow the unary loadings trend when we extrapolate the 1,4-dioxane loadings in the unary simulations using Henry's Law down to the set pressure of 5.8×10^{11} bar for mixture adsorption loadings (Table 2). While unary adsorption trends alone could potentially identify the best framework for adsorption, our method provides accurate estimates of

Framework	Loading @Unary [molec/nm^3]	Loading @512 [molec/nm^3]
FER	5.6×10^{-6}	8.1×10^{-6}
EUO	3.2×10^{-6}	3.9×10^{-6}
IFR	1.5×10^{-6}	1.1×10^{-6}
BEA	4.6×10^{-7}	4.5×10^{-7}
MFI	3.6×10^{-7}	4.1×10^{-7}
MOR	2.0×10^{-7}	2.1×10^{-7}

Table 2: 1,4-dioxane loadings are similar in unary and mixture systems at extrapolated pressure.

selectivity and loadings under specific environmental conditions.

The simulations with large zeolite supercells are feasible with few adsorbates only because of the excellent hydrophobicity of these materials; if much water were to co-adsorb, the simulation would require more water molecules and become computationally expensive. We further verify this by calculating selectivity that also considers water rejection by these zeolite frameworks.

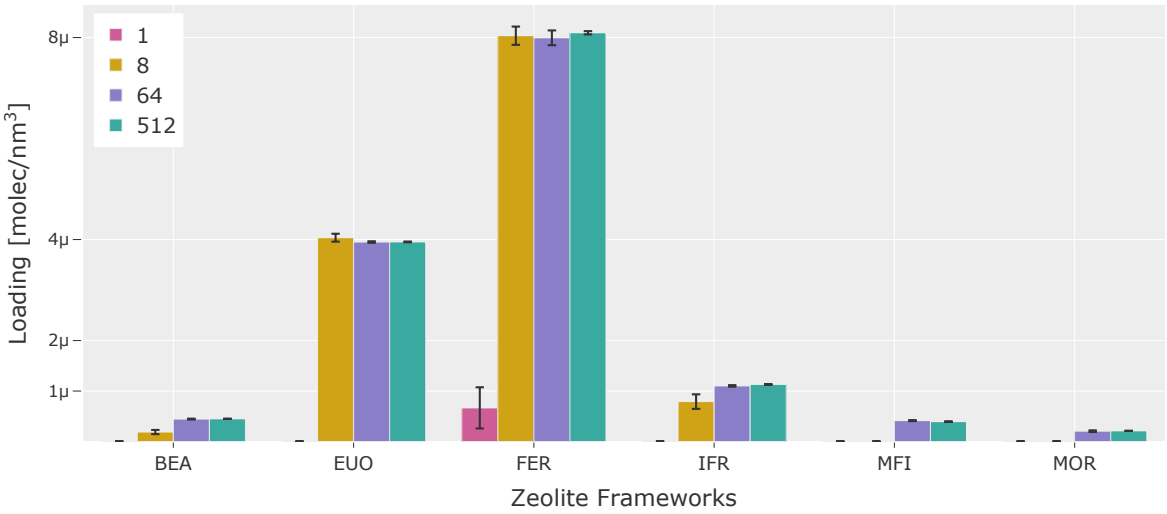

Figure 8: Predicted 1,4-dioxane loading from 0.35 ppb aqueous solution. The x-axis lists the six zeolite frameworks for the four simulation box sizes (1, 8, 64, and 512 times the volume of the minimal simulation box for each framework) with loading in the y-axis.

Selectivity here is defined as the ratio of 1,4-dioxane to water in the zeolite simulation box (Supplementary section 5.5), normalized by the health-based reference concentration of 1,4-dioxane in number ratio, that is:

$$R_c = 0.35 \text{ ppb} = 0.35\ \mu\text{g/L} = \frac{N_{14DX}}{N_{water}} = 7.17 \times 10^{-11} \tag{4}$$

Using this value of R_c, we determine the selectivity as:

$$\text{Selectivity, } S_{ads} = \frac{\left(\frac{N_{14DX}}{N_{water}}\right)_{zeolite}}{R_c} \tag{5}$$

Table 3: Selectivity of the frameworks at 1^3 (1), 2^3 (8), 4^3 (64), and 8^3 (512) times the original unit cell. All values were calculated from each of the eight independent simulations and reported as mean, and uncertainties are reported in subscripts as the standard error of the mean to last significant figures.

Frameworks	S_{ads} @1 ($\times 10^6$)	S_{ads} @8 ($\times 10^6$)	S_{ads} @64 ($\times 10^6$)	S_{ads} @512 ($\times 10^6$)
BEA	0	0.33_8	0.78_2	0.81_1
EUO	0	2.01_4	1.98_2	1.97_1
IFR	0	0.82_2	0.12_3	0.11_1
FER	0.75_5	8.76_2	8.70_2	8.72_4
MFI	0	0	0.24_1	0.23_1
MOR	0	0	0.11_1	0.11_1

Table 3 summarizes the selectivity of 1,4-dioxane for each zeolite framework investigated. All zeolites are extremely selective, with enrichment in the zeolite phase relative to the water phase by at least a factor of 10^5. FER is even more selective, with S_{ads} of 8.7×10^6. Additionally, Figure 9 showcases snapshots of mixture adsorption loadings in FER, varying across different unit cell sizes. The selectivity trends are similar to 1,4-dioxane loadings, with FER being the most selective among others. The selectivity also level-offs after the first scaling of 2^3 of the unit cell volume, indicating the upper limit needed for this concentration of 1,4-dioxane in the mixture.

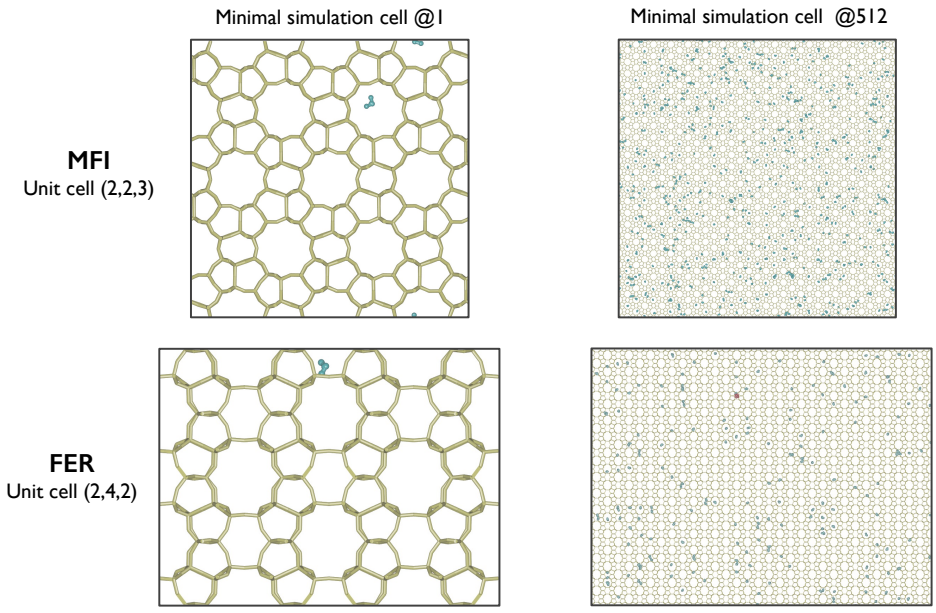

Figure 9: Simulation snapshots from mixture adsorptions show that FER rejects more water than MFI. The water ratio in MFI to FER is 3.8 across the unit cell volumes.

From the number of 1,4-dioxane and water molecules adsorbed in the zeolite framework (Tables 7 and 8), we can determine its efficacy in filtering 1 L of water to produce a 0.35 ppb outlet stream. For example, 1 gram of FER removes 65% of 1,4-dioxane from a feed with a concentration of 0.99 ppb, while the same amount of MOR removes only 5% from a feed concentration of 0.37 ppb. Table 9 in Supplementary section 5.5 lists some predicted amounts of removal for 1, 10, and 100 grams of zeolite for both FER and MOR frameworks.

4 Conclusions and Outlook

Accurately modeling water treatment systems is challenging due to the presence of numerous unknown substances, which vary in their concentrations and often interact with each other. This study addresses two key challenges: identifying effective adsorbents for an emerging water pollutant and sampling the system under environmentally relevant concentrations. This methodology sets the stage for further exploration of effective adsorbents for other emerging contaminants, such as PFAS, arsenic, and chlorinated species. However, the efficacy

of this method is contingent upon both the adsorbent's selectivity for the target pollutant and its ability to reject solvent simultaneously. This stringent requirement limits the approach's applicability to certain types of materials (e.g. very hydrophobic sorbents).

The unary adsorption simulations helped pinpoint frameworks with high-loading capacity and pore-size compatibility with 1,4-dioxane. The investigations uncovered a smaller pore size in the FER framework that snugly accommodates 1,4 dioxane. Furthermore, our mixture adsorption simulations with water indicate that FER possesses exceptional selectivity for low concentrations of 1,4-dioxane; it particularly becomes more apparent in simulations with supercell construction of zeolite frameworks.

The adsorption concentration differs significantly from the environmental concentrations, implying that hydrophobic all-silica zeolites are ultraselective adsorbents, as the latter can be considered to be infinitely diluted. However, it is challenging to synthesize them without defects[19], which enable water coadsorption and would undermine selectivity. This work aims to motivate the synthesis of these zeolites to be used in various separation processes, particularly in water pollutant remediation, where these interactions can play a crucial role. We also achieve large selectivities here while only involving physisorption interactions because of the tight fit of 1,4-dioxane in FER. In other contexts, chemisorption is used to remove trace contaminants from water[76–78] as the means of providing the strong intrinsic interaction to pull the dilute solute from the solution. Traditional Monte Carlo simulations do not have interaction potentials for chemisorption; the development of these could further extend the applicability of this approach.

Acknowledgements

This material is based upon work supported by the National Science Foundation under Grant #2138938, as well as startup funds from the University of Maryland, Baltimore County.

Conflicts of Interest

The authors declare that they have no known competing financial interests or personal relationships that could have appeared to influence the work reported in this paper.

Supporting Information

The supporting information provides additional information on the zeolite frameworks (Section 5.1) and all the force field parameters (Section 5.2), derivation of the expression for the free energy of transfer (5.3), detailed working steps of the thermodynamic extrapolation approach (5.4), and additional tables for analyzing selectivity across the zeolite frameworks(5.5). The simulation source code (version of MCCCS-MN software used in this work), along with sample input files for all the setups (VLCC, gcMC, NPT-Gibbs) and their output files for one independent simulation, is available at `https://github.com/ATOMSLab/14DX_Adsorption`.

References

(1) Deischter, J.; Müller, F.; Bong, B.; Maurer, C.; Hartmann, S. S.; Palkovits, R. *ACS Sustainable Chemistry & Engineering* **2022**, *10*, 10211–10222.

(2) Dauenhauer, P. J.; Abdelrahman, O. A. *ACS Central Science* **2018**, *4*, 1235–1243.

(3) Kumar, S.; Srivastava, R.; Koh, J. *Journal of CO2 Utilization* **2020**, *41*, 101251.

(4) Xu, J.; Xu, Y.; Bu, X.-H. Advances in Emerging Crystalline Porous Materials. 2021.

(5) Corma, A. *Journal of Catalysis* **2003**, *216*, 298–312.

(6) Keil, F. J.; Krishna, R.; Coppens, M.-O. *Reviews in Chemical Engineering* **2000**, *16*, 71–197.

(7) Townsend, R. P.; Coker, E. N. *Studies in Surface Science and Catalysis*; Elsevier, 2001; Vol. 137; pp 467–524.

(8) Margeta, K.; Farkaš, A. *Zeolites-New Challenges* **2020**, 1–10.

(9) Kumar, L.; Kaur, R.; Sharma, J. *Inorganic Chemistry Communications* **2021**, *134*, 108978.

(10) Bolisetty, S.; Peydayesh, M.; Mezzenga, R. *Chemical Society Reviews* **2019**, *48*, 463–487.

(11) Jiménez-Reyes, M.; Almazán-Sánchez, P.; Solache-Ríos, M. *Journal of Environmental Radioactivity* **2021**, *233*, 106610.

(12) Rad, L. R.; Anbia, M. *Journal of Environmental Chemical Engineering* **2021**, *9*, 106088.

(13) Jiang, N.; Shang, R.; Heijman, S. G.; Rietveld, L. C. *Water Research* **2018**, *144*, 145–161.

(14) Cinar, S.; Beler-Baykal, B. *Water Science and Technology* **2005**, *51*, 71–77.

(15) Swenson, P.; Tanchuk, B.; Gupta, A.; An, W.; Kuznicki, S. M. *Desalination* **2012**, *285*, 68–72.

(16) Smit, B.; Maesen, T. L. *Chemical Reviews* **2008**, *108*, 4125–4184.

(17) Baerlocher, C.; McCusker, L. Database of Zeolite Structures. `http://www.iza-structure.org/databases/`.

(18) Cundy, C. S.; Cox, P. A. *Microporous and Mesoporous Materials* **2005**, *82*, 1–78.

(19) Burton, A. W.; Zones, S. I.; Elomari, S. *Current Opinion in Colloid & Interface Science* **2005**, *10*, 211–219.

(20) Anderson, M. A. *Environmental Science & Technology* **2000**, *34*, 725–727.

(21) Pollitt, K. J. G.; Kim, J.-H.; Peccia, J.; Elimelech, M.; Zhang, Y.; Charkoftaki, G.; Hodges, B.; Zucker, I.; Huang, H.; Deziel, N. C., et al. *Science of the Total Environment* **2019**, *690*, 853–866.

(22) Adamson, D. T.; Piña, E. A.; Cartwright, A. E.; Rauch, S. R.; Anderson, R. H.; Mohr, T.; Connor, J. A. *Science of the Total Environment* **2017**, *596*, 236–245.

(23) Mohr, T. K.; DiGuiseppi, W. H.; Hatton, J. W.; Anderson, J. K. *Environmental Investigation and Remediation: 1, 4-dioxane and Other Solvent Stabilizers*; CRC Press, 2020.

(24) McElroy, A. C.; Hyman, M. R.; Knappe, D. R. *Current Opinion in Environmental Science & health* **2019**, *7*, 117–125.

(25) Chiang, S.-Y.; Anderson, R.; Wilken, M.; Walecka-Hutchison, C. *Remediation Journal* **2016**, *27*, 7–27.

(26) Woodard, S.; Mohr, T.; Nickelsen, M. G. *Remediation Journal* **2014**, *24*, 27–40.

(27) Fukuhara, T.; Iwasaki, S.; Hasegawa, T.; Ishihara, K.; Fujiwara, M.; Abe, I. *Journal of Water and Environment Technology* **2011**, *9*, 249–258.

(28) Chen, R.; Liu, C.; Johnson, N. W.; Zhang, L.; Mahendra, S.; Liu, Y.; Dong, Y.; Chen, M. *Chemical Engineering Journal* **2019**, *371*, 193–202.

(29) Sherman, J. D. *Proceedings of the National Academy of Sciences* **1999**, *96*, 3471–3478.

(30) Wragg, D. S.; Morris, R. E.; Burton, A. W. *Chemistry of Materials* **2008**, *20*, 1561–1570.

(31) Smit, B.; Krishna, a. *Chemical Engineering Science* **2003**, *58*, 557–568.

(32) Fuchs, A. H.; Cheetham, A. K. *The Journal of Physical Chemistry B* **2001**, *105*, 7375–7383.

(33) Catlow, C. R. A.; Bell, R.; Gale, J.; Lewis, D. *Studies in Surface Science and Catalysis*; Elsevier, 1995; Vol. 97; pp 87–100.

(34) Catlow, C. R. A.; Smit, B.; van Santen, R. *Computer Modelling of Microporous Materials*; Elsevier, 2004.

(35) Neimark, A. V.; Vishnyakov, A. *Physical Review E* **2000**, *62*, 4611.

(36) Vishnyakov, A.; Neimark, A. V. *The Journal of Physical Chemistry B* **2001**, *105*, 7009–7020.

(37) Neimark, A. V.; Vishnyakov, A. *The Journal of Chemical Physics* **2005**, *122*, 234108.

(38) Clark, M. D.; Morris, K. R.; Tomassone, M. S. *Langmuir* **2017**, *33*, 9081–9090.

(39) Gor, G. Y.; Rasmussen, C. J.; Neimark, A. V. *Langmuir* **2012**, *28*, 12100–12107.

(40) Neimark, A. V.; Vishnyakov, A. *The Journal of Chemical Physics* **2005**, *122*, 174508.

(41) Zheng, F.; Zhang, X.; Wang, W. *Langmuir* **2008**, *24*, 4661–4669.

(42) Luo, J.; Farrell, J. *Environmental Science & Technology* **2003**, *37*, 1775–1782.

(43) Siepmann, J.; Martin, M.; Chen, B.; Wick, C.; Stubbs, J.; Potoff, J.; Eggimann, B.; McGrath, M.; Zhao, X.; Anderson, K., et al. Monte Carlo for Complex Chemical Systems—Minnesota. 2017.

(44) Panagiotopoulos, A. Z. *Molecular Physics* **1987**, *61*, 813–826.

(45) Smit, B. d.; De Smedt, P.; Frenkel, D. *Molecular Physics* **1989**, *68*, 931–950.

(46) Panagiotopoulos, A. Z.; Quirke, N.; Stapleton, M.; Tildesley, D. *Molecular Physics* **1988**, *63*, 527–545.

(47) Ben-Naim, A. Y. *Statistical Thermodynamics for Chemists and Biochemists*; Springer Science & Business Media, 2013.

(48) Martin, M. G.; Siepmann, J. I. *Theoretical Chemistry Accounts* **1998**, *99*, 347–350.

(49) Transferable Potentials for Phase Equilibria. `http://trappe.oit.umn.edu/`.

(50) Keasler, S. J.; Charan, S. M.; Wick, C. D.; Economou, I. G.; Siepmann, J. I. *The Journal of Physical Chemistry B* **2012**, *116*, 11234–11246.

(51) Bai, P.; Tsapatsis, M.; Siepmann, J. I. *The Journal of Physical Chemistry C* **2013**, *117*, 24375–24387.

(52) Jorgensen, W. L.; Chandrasekhar, J.; Madura, J. D.; Impey, R. W.; Klein, M. L. *The Journal of Chemical Physics* **1983**, *79*, 926–935.

(53) Chen, B.; Siepmann, J. I. *The Journal of Physical Chemistry B* **2006**, *110*, 3555–3563.

(54) Rafferty, J. L.; Siepmann, J. I.; Schure, M. R. *Analytical Chemistry* **2008**, *80*, 6214–6221.

(55) Rafferty, J. L.; Sun, L.; Siepmann, J. I.; Schure, M. R. *Fluid Phase Equilibria* **2010**, *290*, 25–35.

(56) Shah, M. S.; Tsapatsis, M.; Siepmann, J. I. *Langmuir* **2015**, *31*, 12268–12278.

(57) Pahari, S.; Dorneles de Mello, M.; Shah, M. S.; Josephson, T. R.; Ren, L.; Nguyen, H. G. T.; Van Zee, R. D.; Tsapatsis, M.; Siepmann, J. I. *ACS Physical Chemistry Au* **2021**, *2*, 79–88.

(58) Dubbeldam, D.; Torres-Knoop, A.; Walton, K. S. *Molecular Simulation* **2013**, *39*, 1253–1292.

(59) Allen, M. P.; Tildesley, D. J. *Computer Simulation of Liquids*; Oxford University Press, 2017.

(60) Metropolis, N.; Rosenbluth, A. W.; Rosenbluth, M. N.; Teller, A. H.; Teller, E. *The journal of Chemical Physics* **1953**, *21*, 1087–1092.

(61) Siepmann, J. I. *Molecular Physics* **1990**, *70*, 1145–1158.

(62) Siepmann, J. I.; Frenkel, D. *Molecular Physics* **1992**, *75*, 59–70.

(63) Martin, M. G.; Siepmann, J. I. *The Journal of Physical Chemistry B* **1999**, *103*, 4508–4517.

(64) Calero, S. *Comprehensive Inorganic Chemistry II (Second Edition): From Elements to Applications*; Elsevier Ireland Ltd, 2013; pp 989–1006.

(65) Vlugt, T.; Martin, M.; Smit, B.; Siepmann, J.; Krishna, R. *Molecular Physics* **1998**, *94*, 727–733.

(66) Martin, M. G.; Thompson, A. P. *Fluid Phase Equilibria* **2004**, *217*, 105–110.

(67) Martin, M. G.; Biddy, M. J. *Fluid Phase Equilibria* **2005**, *236*, 53–57.

(68) Martin, M. G.; Frischknecht, A. L. *Molecular Physics* **2006**, *104*, 2439–2456.

(69) Wick, C. D.; Siepmann, J. I. *Macromolecules* **2000**, *33*, 7207–7218.

(70) Linstrom, P.; W.G. Mallard, E. NIST Chemistry WebBook, NIST Standard Reference Database Number 69, National Institute of Standards and Technology, Gaithersburg MD, 20899. `https://doi.org/10.18434/T4D303`, [retrieved October 20, 2023].

(71) Chen, B.; Siepmann, J. I. *The Journal of Physical Chemistry B* **1999**, *103*, 5370–5379.

(72) Chodera, J. D. *Journal of Chemical Theory and Computation* **2016**, *12*, 1799–1805.

(73) DeJaco, R. F.; Bai, P.; Tsapatsis, M.; Siepmann, J. I. *Langmuir* **2016**, *32*, 2093–2101.

(74) Yang, Y.; Bai, P.; Guo, X. *Industrial & Engineering Chemistry Research* **2017**, *56*, 14725–14753.

(75) Bereciartua, P. J.; Cantín, Á.; Corma, A.; Jordá, J. L.; Palomino, M.; Rey, F.; Valencia, S.; Corcoran Jr, E. W.; Kortunov, P.; Ravikovitch, P. I., et al. *Science* **2017**, *358*, 1068–1071.

(76) Rajaković, L. V.; Mitrović, M. M. *Environmental Pollution* **1992**, *75*, 279–287.

(77) Renu, M. A.; Singh, K.; Upadhyaya, S.; Dohare, R. *Materials Today: Proceedings* **2017**, *4*, 10534–10538.

(78) Gagliano, E.; Sgroi, M.; Falciglia, P. P.; Vagliasindi, F. G.; Roccaro, P. *Water Research* **2020**, *171*, 115381.

(79) Newsam, J.; Treacy, M. M.; Koetsier, W.; Gruyter, C. d. *Proceedings of the Royal Society of London. A. Mathematical and Physical Sciences* **1988**, *420*, 375–405.

(80) Briscoe, N.; Johnson, D.; Shannon, M.; Kokotailo, G.; McCusker, L. *Zeolites* **1988**, *8*, 74–76.

(81) Morris, R. E.; Weigel, S. J.; Henson, N. J.; Bull, L. M.; Janicke, M. T.; Chmelka, B. F.; Cheetham, A. K. *Journal of the American Chemical Society* **1994**, *116*, 11849–11855.

(82) Barrett, P.; Camblor, M.; Corma, A.; Jones, R.; Villaescusa, L. *Chemistry of Materials* **1997**, *9*, 1713–1715.

(83) Van Koningsveld, H.; Jansen, J.; Van Bekkum, H. *Zeolites* **1987**, *7*, 564–568.

(84) Abascal, J. L.; Vega, C. *The Journal of Chemical Physics* **2005**, *123*.

5 Supporting Information

5.1 Zeolite Frameworks

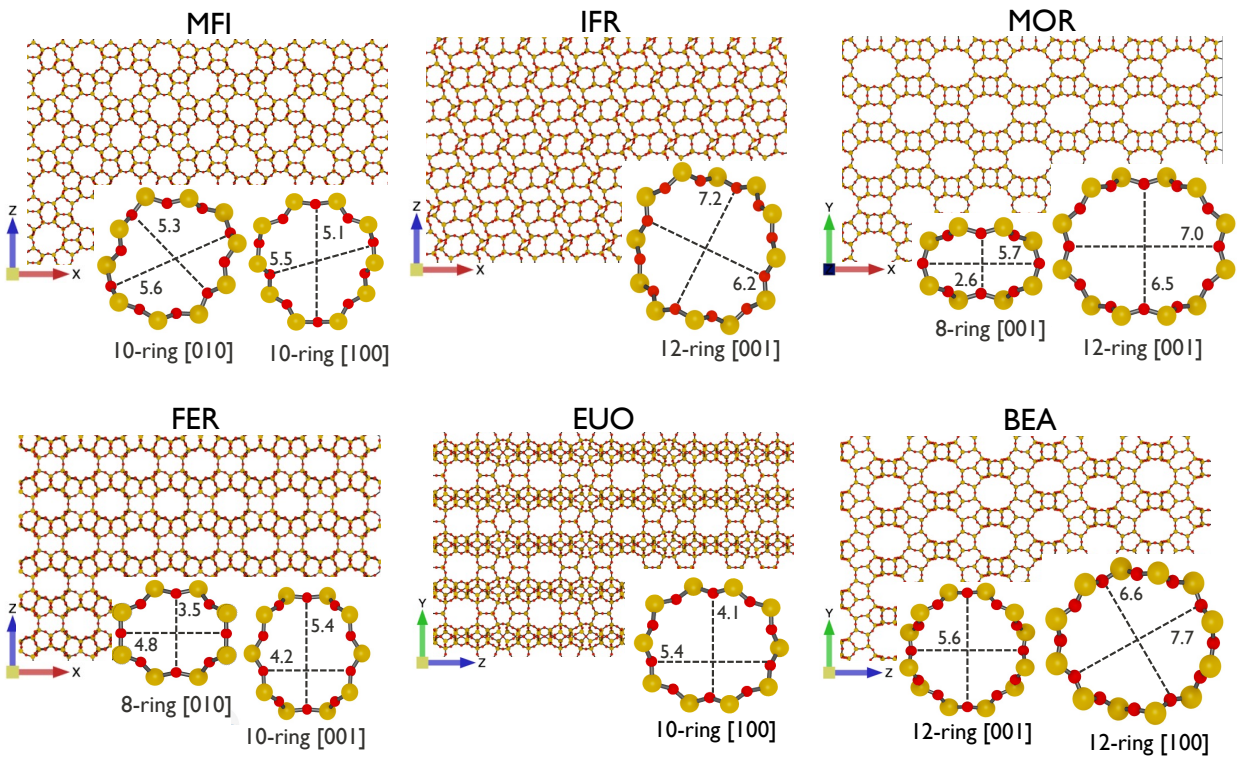

Figure 10: The zeolite frameworks investigated in this study, with their pore size and structures (not to scale).

Table 4: Zeolite Unit Cell Parameters

Framework	a [Å]	b [Å]	c [Å]	α [deg]	β [deg]	γ [deg]	unit cell [x,y,z]	refs
BEA	12.6614	12.6614	26.4061	90.00	90.00	90.00	$[3 \times 3 \times 2]$	[79]
EUO	13.6950	22.3260	20.1780	90.00	90.00	90.00	$[2 \times 2 \times 2]$	[80]
FER	14.0703	7.4197	18.7200	90.00	90.00	90.00	$[2 \times 4 \times 2]$	[81]
IFR	18.6524	13.4960	7.6311	90.00	101.98	90.00	$[2 \times 3 \times 4]$	[82]
MFI	20.0220	19.8990	13.3830	90.00	90.00	90.00	$[2 \times 2 \times 3]$	[83]
MOR	18.2560	20.5340	7.5420	90.00	90.00	90.00	$[2 \times 2 \times 4]$	[17]

5.2 Force field parameters

Table 5: Force field parameters of 1,4-dioxane, water and zeolite

parameters for non bonded potentials					
type	pseudo atom	σ [Å]	ϵ/k_B [K]	q [e]	refs
CH_2–[O]–CH_2–CH_2	O	2.39	155.0	−0.38	[50]
O–[CH_2]–CH_2–O	CH_2	3.91	52.5	0.19	[50]
H–[O]–H	O	3.154	78.0	0	[84]
[H]–O–H	H	0	0	0.52	[84]
H_2O–[M]	M	0	0	−1.04	[84]
[Si]–O	Si	2.30	22.0	1.50	[51]
Si–[O]	O	3.30	53.0	−0.75	[51]
parameters for bonded potentials					
fixed bond	length [Å]				refs
CH_x–CH_y	1.5400				[50]
CH_2–O	1.4100				[50]
H–O–H	0.9572				[84]
bend angle	k_θ/k_B [K/rad^2]		θ_0 [deg]		refs
CH_x–(CH_y)–O	25150		112		[50]
CH_x–(O)–CH_y	30200		112		[50]
torsion	c_0/k_B [K]	c_1/k_B [K]	c_2/k_B [K]	c_3/k_B [K]	refs
O–(CH_2)–(CH_2)–O	13537	10876	5223	−123	[50]
CH_2–(CH_2)–(O)–CH_2	7037	14958	7606	1546	[50]

5.3 Free Energy of Transfer

When examining phase separation, the most suitable thermodynamic parameter is the chemical potential, μ, at equilibrium. In all phases, μ remains the same, and any change in μ will affect the flow from one phase to another. For two phases, α and β, in which a solute

molecule, **s**, is distributed, if both phases are at the same temperature and pressure, the chemical potential of **s** will be identical in both phases. This can be expressed as follows:

$$\mu_s^{\alpha} = \mu_s^{\beta} \tag{6}$$

Applying the chemical potential formula for solvation where we impose very low concentrations of **s** in both phases, we get

$$\mu_s^{*\alpha} + kT(\ln \rho_s^{\alpha}) = \mu_s^{*\beta} + kT(\ln \rho_s^{\beta}) \tag{7}$$

Here k, T, and ρ are Boltzmann constant, temperature, and number density of **s** in each phase. By rearrangement, we can write the solvation of Gibbs free energies as

$$\Delta G_s^{*\beta} - \Delta G_s^{*\alpha} = (\mu_s^{*\beta} - \mu_s^{*ig}) - (\mu_s^{*\alpha} - \mu_s^{*ig}) \tag{8}$$

which is,

$$\Delta G_s^{*\beta} - \Delta G_s^{*\alpha} = \mu_s^{*\beta} - \mu_s^{*\alpha} = kT[\ln\left(\frac{\rho_s^{\alpha}}{\rho_s^{\beta}}\right)_{eq}] \tag{9}$$

Now, when the phase α is an ideal gas, $\Delta G_s^{*\alpha} = 0$, thus equation 9 reduces to:

$$\Delta G_s^{*\beta} = kT[\ln\left(\frac{\rho_s^{ig}}{\rho_s^{\beta}}\right)_{eq}] \tag{10}$$

For a system in which the vapor and liquid phases of a pure component are in equilibrium, we can determine the solvation Gibbs energy of the component in its pure liquid state, provided that the vapor pressure is sufficiently low to be considered an ideal gas.

If **s** is very dilute in phase β, the limiting form of the equation is:

$$\Delta G_s^{*0} = kT[\ln\left(\frac{\rho_s^{ig}}{\rho_s^{\beta}}\right)_{eq}] \tag{11}$$

and therefore, the Gibbs free energy of transfer from the mixture of a dilute solution of 1,4-dioxane in water to gauge cell (GC) is:

$$\Delta G^{*0}_{14DX} = kT[\ln\left(\frac{\rho^{GC}_{14DX}}{\rho^{mix}_{14DX}}\right)_{eq}] \tag{12}$$

5.4 Gauge Cell Extrapolation

The extrapolation from the gauge cell simulations is described here.

Table 6: Health-based reference concentration (R_c) in different units

Value	Unit
0.35	ppb
0.35	μg/L
2.39×10^{-9}	molec/nm^3

The mean free energy of transfer for the six state points with the lowest 1,4-dioxane concentrations is:

$$\overline{\Delta G^{*0}_{14DX}} = -9.2\,\text{kJ/mol} \tag{13}$$

Using this value for ΔG^{*0}_{14DX} and reference concentration 2.39×10^{-9} molec/nm^3 in Equation 5.3, we get concentration in gauge cell at 300 K as:

$$\rho^{GC}_{14DX} = 6.11 \times 10^{-11}\,\text{molec/nm}^3 \tag{14}$$

We then plot the pressure in the gauge cell versus the concentration in the main cell.

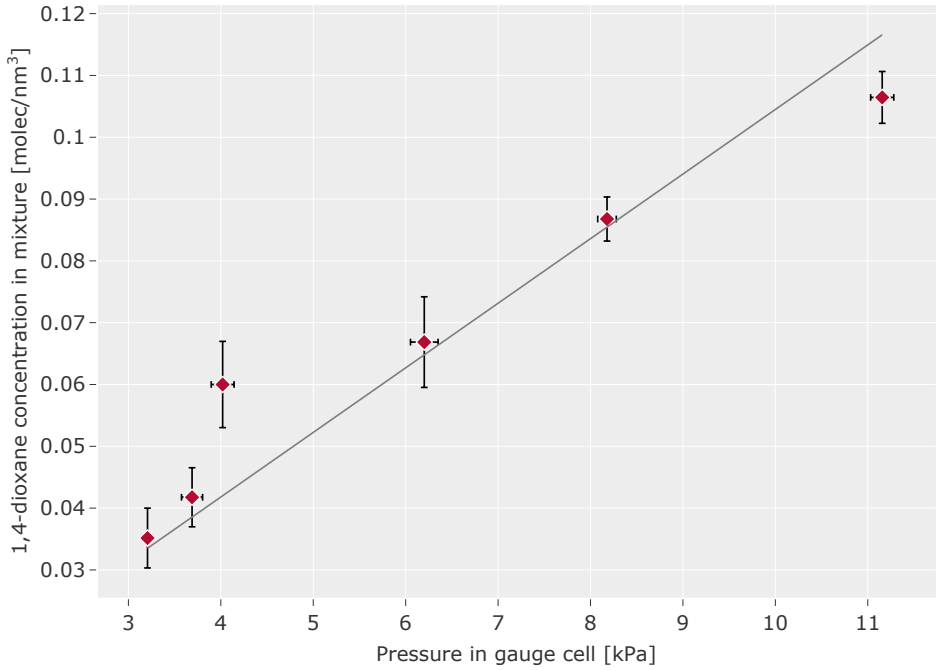

Figure 11: 1,4-dioxane concentration versus pressure in the gauge cell. Since the concentrations are extremely low, and the relationship is linear within the uncertainty limits, we can equate the slope as Henry's constant for extrapolation.

To calculate the slope of the straight line in Figure 11, we fit the points using linear regression and setting the intercept as zero. This gives us a slope of 0.0105 with units of molec / (nm^3 kPa). Using this slope, we then extrapolate the pressure for reference concentration as:

$$\begin{aligned} \rho_{14DX}^{GC} &= H \times P \\ P &= \frac{\rho_{14DX}^{GC}}{H}\ (\text{kPa}) \\ P &= 5.8 \times 10^{-9}\ \text{kPa} \\ P &= 5.8 \times 10^{-11}\ \text{bar} \end{aligned} \tag{15}$$

The pressure calculation in the gauge cell for water is straightforward, as it is just the

average of all the simulation state points conducted, which is 4.5 kPa or 4.5×10^{-2} bar.

5.5 Selectivity

Table 7: Mean number of 1,4-dioxane molecules inside zeolite simulation boxes from eight independent simulations. Uncertainties are reported as the standard error of mean in subscript for the last significant figure.

Frameworks	N_{14DX}@1	N_{14DX}@8	N_{14DX}@64	N_{14DX}@512
BEA	0	0.00011_3	0.00217_4	0.01754_4
EUO	0	0.00159_3	0.01248_5	0.0999_2
FER	0.00002_1	0.00201_5	0.0160_3	0.1296_5
IFR	0	0.00029_5	0.00325_4	0.02669_7
MFI	0	0	0.00170_4	0.01291_8
MOR	0	0	0.00059_5	0.00490_3

Table 8: Mean number of water molecules inside zeolite simulation boxes from eight independent simulations. Uncertainties are reported as the standard error of mean in subscript for the last significant figure.

Frameworks	N_{water}@1	N_{water}@8	N_{water}@64	N_{water}@512
BEA	0.96_2	4.95_1	38.7_5	303.3_2
EUO	1.36_2	11.07_5	87.9_7	705.8_3
FER	0.400_3	3.20_2	25.7_2	207.3_5
IFR	0.60_1	5.1_2	39.0_8	327.8_1
MFI	1.51_3	11.9_2	97.5_6	781.8_2
MOR	1.21_1	9.46_5	76.9_4	613.9_1

Table 9: Predicted fractional removal for different zeolite amounts and frameworks to output health-based reference concentration of 0.35 ppb 1,4-dioxane filtering 1 L of contaminated water for zeolite minimal simulation cell @64.

Framework	Zeolite Weight (g)	Feed Stream Conc. (ppb)	Fraction removed	Outlet Conc. (ppb)
FER	1	0.99	0.645	0.35
	10	6.71	0.948	0.35
	100	64.0	0.995	0.35
MOR	1	0.37	0.048	0.35
	10	0.53	0.336	0.35
	100	2.12	0.835	0.35